CHEMISTRY
A EUROPEAN JOURNAL

DOI: 10.1002/chem.200801146

Exploring the Structural Complexities of Metal–Metalloid Nanoparticles: The Case of Ni·B as Catalyst

Junfeng Geng,* David A. Jefferson, and Brian F. G. Johnson*[a]

Abstract: Understanding of the structural complexities of metal–metalloid nanoparticles is at the heart of several proposals for investigating the physical properties and practical applications of these bi-elemental nanomaterials. To date, the most widely studied metal–metalloid is the nickel–boron (Ni·B) system; however, the exact nature of the structure of the material itself has remained unclear. Herein we show our systematic investigations of the material in an attempt to reveal its fascinating nanostructure. The relation between its high catalytic activity and the ultrafine structure is explored, and the work has been further extended to the formation of colloidal Ni·B nanoparticles. The results presented in this work may represent a substantial progress toward a full understanding of the nickel–boron chemistry.

Keywords: boron · catalysts · nanomaterials · nanostructures · nickel

Introduction

The current development in catalysis of nanoparticles has stimulated a renewed interest in catalysts that display high catalytic activity and selectivity for hydrogenation or dehydrogenation reactions.[1] Previously, the nickel–boron nanomaterial (denoted as Ni·B), which was initially produced in the 1950s by chemical reduction of an appropriate nickel salt by alkali metal borohydrides,[2] has been shown to have an exceedingly high catalytic activity for a wide range of hydrogenations and dehydrogenations.[2,3] The catalyst has been demonstrated to be at least as active as standard Raney nickel but produces less double-bond migration than the latter in hydrogenations.[2–5] Similar catalysts produced from alternative reduction media have been shown to be highly selective for certain hydrogenations of one double bond in the presence of another.[6] Importantly, these catalysts are known to be more easily prepared than Raney nickel, with a high degree of reproducibility and reliability.

The remarkable catalytic properties of the material have given rise to extensive studies that so far include reaction kinetics,[7,8] stoichiometric chemistry,[9–11] chemical state of the surface,[12–14] and the catalytic applications.[15–18] In addition, studies on the Ni·B system have been widely extended to other similar metal–metalloid materials, which involve transition metals and the elements of B and P to form Fe·B, Co·B, Pd·B, Ni·P, Fe·P, Fe·Ni·B, Ni·Fe·P, Fe·P·B, Ni·W·P, Pt·B, Ni·P·B, or Ni·Co·B.[19–22] These studies have led to important applications not only in catalysis but also in other fields such as in deuterium exchange,[23] selective desulfurizations,[24] and for the preparation of magnetic recording materials, ferrofluids, and chemical composites.[25]

Despite the important properties and applications, however, the precise nature of the nickel–boron material itself has always remained unclear. It was originally thought that this material was a simple stoichiometric nickel boride compound, with a formula of Ni_2B or Ni_3B, but the boron content was later found to vary with the ratio of the reactants used in preparation.[7–18] Studies on the structure using powder X-ray diffraction (XRD),[13,26–28] X-ray photoelectron spectroscopy (XPS),[12,14,29,30] and transmission electron microscopy (TEM)[15,27,28,30] led to a view that the material is amorphous, and as a consequence, it is frequently referred to as an "amorphous nickel boron alloy".

In a recent communication,[31] we reported on our investigations of the Ni·B catalyst prepared by using the chemical reduction method. We were able to show that the material is not a simple nickel boride compound but a mixture of metallic nickel and a boron-containing substance. More importantly, we found that rather than being amorphous, the material possesses a highly unusual nanostructure in which

[a] Dr. J. Geng, Dr. D. A. Jefferson, Prof. B. F. G. Johnson
Department of Chemistry
University of Cambridge
Cambridge, CB2 1EW (United Kingdom)
Fax: (+44) 1223-336362
E-mail: jg201@cam.ac.uk
bjohnson@freenet.co.uk

Supporting information for this article is available on the WWW under http://dx.doi.org/10.1002/chem.200801146.

very small Ni nanoparticles (1–3 nm) form a cluster arrangement that serves as a host to guest B-containing species accommodated within their interstitial sites. In the present work, we show the formation of alternative Ni•B structures prepared under different conditions, and offer an explanation of their varying catalytic activity on the basis of their structural characteristics. The work has been further extended to the preparation and examination of colloidal Ni•B nanoparticles, which are largely different from the original material.

Results and Discussion

Nickel–boron catalytic precipitate: The synthesis of the material was carried out in aqueous solution according to a literature method using nickel acetate ($Ni(CH_3COO)_2{\cdot}4H_2O$) and sodium borohydride ($NaBH_4$).[2] Examination of the product by SEM showed that the material consists of nanoparticles with a typical size of approximately 30 nm (Figure 1), consistent with the TEM examination (Figure 2a). Detailed observation using high-resolution TEM (HRTEM) revealed that these nanoparticles were not amorphous but possessed an ultrafine crystalline structure (Figure 2b and c). Each particle was itself an aggregate of a large number of smaller component nanoparticles with a size of 1–3 nm. These tiny components, although extremely small, with the smallest showing only five lattice fringes, were nevertheless clearly crystalline. They were very tightly clustered together such that each complete aggregate particle was clearly separated from its neighbors. This structure was in marked contrast to that of conventional nickel colloids, which are usually well-defined single crystals. Within the networks of gaps formed by the nanoparticles, and around the complete ensemble, a second amorphous phase was observed; this appears to prevent further sintering of the crystalline nanoparticles.

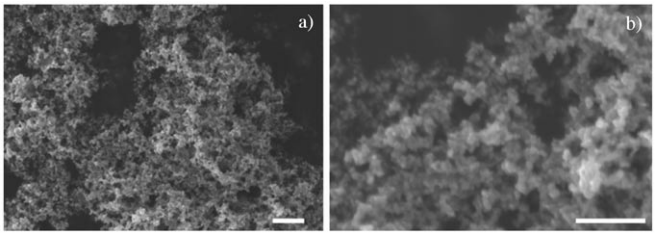

Figure 1. SEM images of the as-made Ni–B particulate precipitate yielded from the reaction of $Ni(CH_3COO)_2$ with $NaBH_4$ in aqueous solution: a) lower and b) higher magnification images of the same sample. Scale bars: 300 nm.

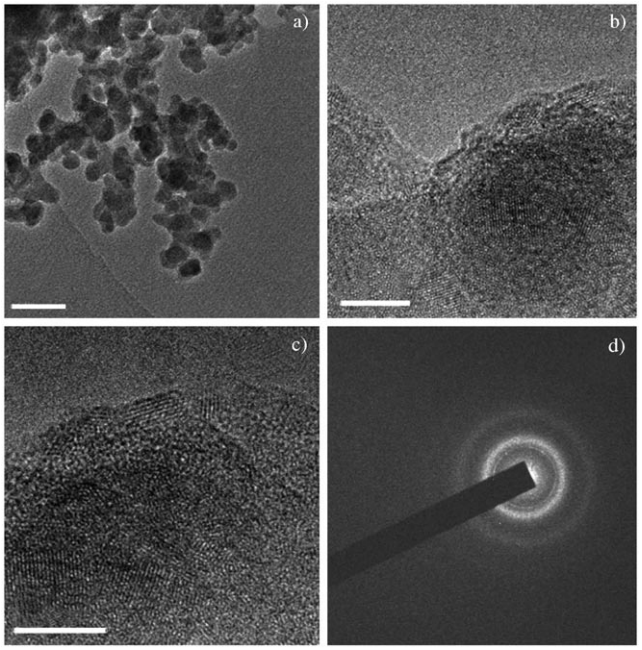

Figure 2. TEM images of the nickel–boron nanoparticles as a precipitate yielded from the reaction of $Ni(CH_3COO)_2$ with $NaBH_4$ in aqueous solution: a) A low magnification image shows the size and the morphology of the nanoparticles (scale bar: 50 nm). b) A higher magnification (×600k) image of a typical particle in the precipitate (scale bar: 5 nm). c) The image of (b) at a higher resolution (×800k), to show the lattice fringes of the component nickel crystallites with varied orientations (scale bar: 5 nm). d) The nano-beam electron diffraction rings of the sample.

Previous studies using XPS have found that the binding energy of Ni $2p_{3/2}$ in this material is in line with that of the bulk nickel (≈852.5 eV),[12,14,30] implying the elemental state for the metal. However, as regards the boron involved, two forms appear to be present, corresponding to a binding energy of B 1s at 188.2 and 191.7 eV. These two forms were assigned to the elemental boron associated with the nickel, and the residual boron in the deposited BO_2^- ions that are produced by the hydrolysis of $NaBH_4$.[12] In similar products from the systems of Pd•B and Pt•B, a third form of boron with a characteristically low binding energy of approximately 182 eV, which is believed to arise from a hydrogen-containing boron species (denoted as B–H), has also been observed.[9,12] From considering these findings, we expect that in our sample, the observed component crystallites are of metallic nickel, and the captive surface phase is of a boron-containing species.

To test this hypothesis, we first imaged many nanoparticles at random and avoided any long-time exposure of individual particles to the electron beam. These observations yielded a consistent result that all particles possessed the same nanostructure. Nano-beam selected-area electron diffraction (SAED) patterns were then recorded for many particles within the sample. We chose the SAED rather than the power spectra of the high-resolution images because the former has the advantage of providing more detailed information, whereas in the latter the radial distribution function could be masked by the rings arising from the Fourier transform of the phase contrast transfer function (PCTF) of the microscope.[32] Furthermore, nano-beam diffraction patterns are not subject to the information limit of the microscope in imaging mode. The recorded diffraction pattern shows three

rings, an inner relatively sharp ring, a stronger but more diffuse middle one, and a similarly diffuse outer ring (Figure 2d). The *d* spacing of the corresponding lattices was determined to be as follows: inner, 2.506 Å; middle, 2.094 Å; and outer, 1.231 Å. The strong middle ring could correspond to either the Ni(111) or NiO(200) diffraction lines, and the outer ring to Ni(220) or NiO(311). The inner sharp ring does not fit any known line of these phases, but matches exactly the forbidden (110) spacing of metallic nickel. Given the extremely small size of the particles, and the strong interaction of 300 kV electrons with matter, it is highly probable that the normal systematic absence conditions break down and this diffraction ring is thereby allowed. Moreover, the absence of the (111) and (220) lines of nickel oxide in the diffraction pattern suggests that the particles are not the oxide but almost certainly metallic nickel. This does not completely rule out the possibility of nickel boride, but with the latter, larger *d* spacings would also be expected. These, however, were not observed.

Powder X-ray diffraction (XRD) studies on both the as-prepared and thermally annealed samples were then performed. The results are shown in Figure 3. As expected, the

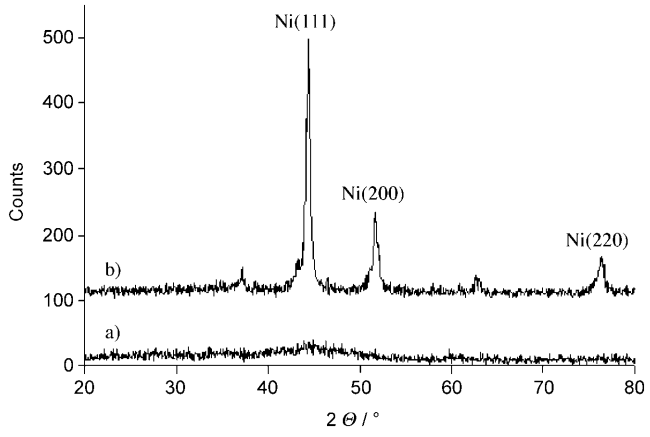

Figure 3. XRD profiles of a) the as-prepared nickel–boron nanoparticles and b) the thermally annealed sample at 600 °C under an argon atmosphere. The assigned diffraction peaks in (b), from left to right, correspond to the *d* spacing of 2.03, 1.73, and 1.25 Å, respectively, for metallic nickel.

raw material shows a complete absence of any sharp diffraction peaks, and only a broad diffraction at around $2\theta = 45°$ (Figure 3a), consistent with the literature reports.[13,26–28] Moreover, in previous studies this broad peak has been assigned to amorphous nickel. Here, our HRTEM observation of the ultrafine crystalline structure clearly indicates that although the component nanoparticles are extremely small, they are nevertheless crystalline. Almost certainly, this broad diffraction arises from a superposition of the broadened lines from these extremely small component nanoparticles, particularly as it is centered at the position of the Ni(111) peak ($d = 2.02$–2.04 Å).[33] Thermal treatment of the sample at 600 °C in argon dramatically improved the quality of the XRD profile, which suggests increased crystallization by sintering of the small crystals. The three strongest diffraction lines of metallic nickel were then fully developed (Figure 3b), corresponding to the 2θ values of 44.45, 51.73, and 76.84°, and matching exactly the metal Ni(111), Ni(200), and Ni(220) lines, respectively.[34,35] This result was subsequently confirmed by the HRTEM examination of the annealed sample, in which larger metallic Ni nanoparticles were clearly observed (Figure 4). On the basis of these findings, we conclude that the component nanoparticles are of metallic nickel.

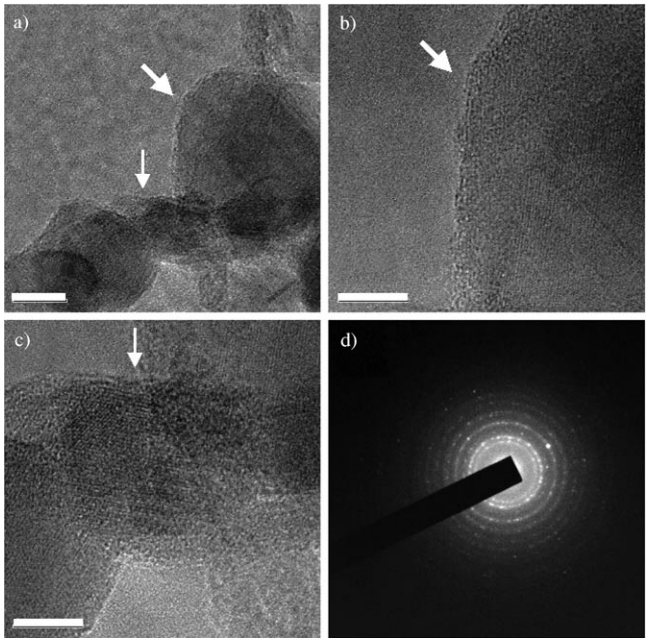

Figure 4. TEM images of a thermally annealed (600 °C under argon) Ni–B precipitate specimen to show the sintered metallic Ni crystals. a) A low magnification image (scale bar: 10 nm); b) and c) HRTEM images corresponding to the particles shown by the arrows in (a) to show their crystal fringes (scale bars: 5 nm); d) the SAED pattern of the sample corresponding to the *fcc* structure of metallic nickel.

Energy dispersive X-ray spectroscopy (EDS) measurements were performed on the as-prepared specimen to confirm its composition, and in particular, to determine the role of boron in the specimen. A parallel study of microcrystalline nickel oxide confirmed that the low O(K edge) emission peaks from the specimen were not compatible with the presence of appreciable nickel oxide. As boron is difficult to detect because of its low emission energy (≈ 188 eV), a preliminary investigation was carried out on B_2O_3 to ascertain the detection limit (see Figure 1 in the Supporting Information). To avoid reduction in the electron beam, this investigation utilized large diameter beams (1–10 μm) and the spectra were recorded from the same area after different irradiation times to test for consistency. Under these conditions, no sample reduction was observed. The observed boron K emission from the catalyst is shown in Figure 5. Multiple EDS analyses yielded a mean peak O(K edge)/B(K

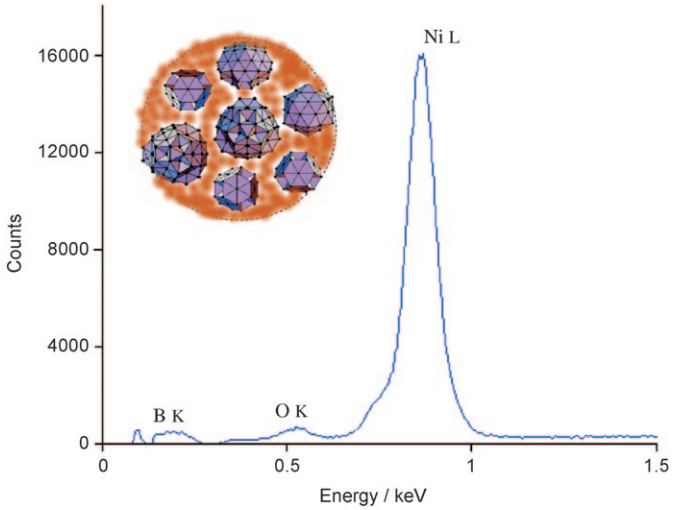

Figure 5. An EDS spectrum showing the elements involved in the material and their corresponding X-ray emission peaks. Inset: a schematic diagram shows the fine nanostructure of the Ni–B particles. It is made up of a cluster of tiny nickel single crystallites (1–3 nm) as the host that appear to hold a boron-containing species in their interstitial spaces.

edge) ratio of approximately 1.0, far smaller than that obtained from B_2O_3, which is approximately 13.9. This result indicates that the boron in the sample is not an oxide, but probably elemental boron associated with the nickel, together with some deposited BO_2^- ions.

To more fully justify the above views, XPS measurements of Ni $2p_{3/2}$ and B 1s were also performed and the results are shown in Figure 6. It can be seen that the Ni $2p_{3/2}$ binding energy, (852.3 ± 0.01) eV, is consistent with that for bulk metallic nickel, further supporting our conclusion that the nickel in the catalyst is nickel metal. This test is also in a good agreement with the literature on NiB,[12,14,30] and the XPS data for other metals such as measurements for the Co $2p_{3/2}$, Fe $2p_{3/2}$, Pd $3d_{5/2}$, and Pt $4f_{7/2}$ levels in the corresponding M–B-type catalysts.[9,12]

The surface oxidation of the nickel metal was observed, and the corresponding XPS peak was at 855.7 eV, in agreement with the XRD data in which a small amount of nickel oxide was present (Figure 3 and ref. [34]). The surface oxidation of nickel has also been reported by Okamoto et al. and Vedrine et al. on the basis of their XPS measurements.[12,36] In addition, the small XPS peak at 860.9 eV may be attributed to the contamination of $Ni(CH_3COO)_2$ as the reactant employed, and this can be further seen by our detailed XPS scans of C 1s and O 1s peaks for the sample (see Figures 4 and 5 in the Supporting Information).

As for the surface boron, two types of boron denoted as B-1 and B-2 were observed with their corresponding B 1s binding energies of 187.4 and 191.0 eV, respectively (Figure 6, lower spectrum). The B-1 species can be readily assigned to the amorphous boron combined with the nickel as observed in the HRTEM, since the binding energy corresponds very closely to that of elemental boron (186.7 eV). This boron species can be easily differentiated from boron

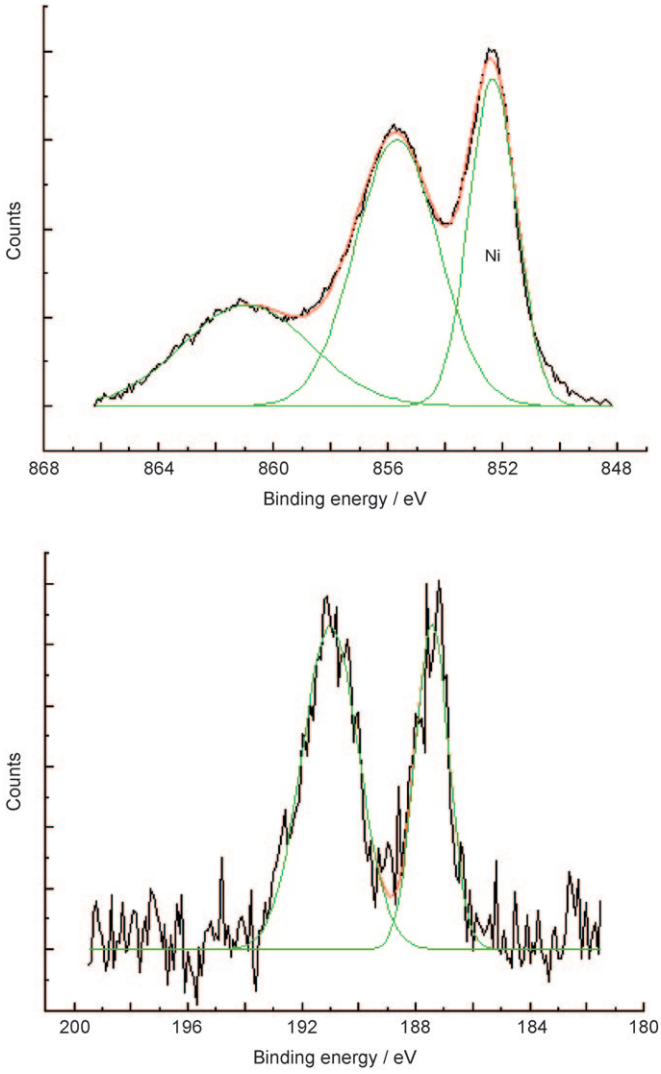

Figure 6. XPS measurements of the spectra of Ni $2p_{3/2}$ (upper) and B 1s (lower) for the Ni•B catalyst (pass energy: 20 eV). The black lines correspond to the raw data, whereas the red and green lines are the smoothed profiles and the fits to the individual peaks, respectively.

oxide based on their large difference in binding energy. The B-2 species may arise from the deposited BO_2^- because of the hydrolysis of $NaBH_4$ (also see the kinetic reaction equations below), a result that is in a good agreement with those obtained by Schreifels et al. and Okamoto et al.[12,14]

Based on all these results, a schematic diagram illustrating the nanostructure of the particulate nickel–boron precipitate was constructed, and this is shown by the inset of Figure 5.

Formation of the bi-elemental particles should result from a coreduction of the two elements in the solution, and this may be further understood from the kinetics of the hydrolysis of BH_4^- ions and the reaction of BH_4^- with Ni^{2+}, which has been proven to follow three independent equations [Eqs. (1)–(3)]:[7,8,10]

$$BH_4^- + 2\,H_2O \rightarrow BO_2^- + 4\,H_2 \quad (1)$$

$$BH_4^- + 2\,Ni^{2+} + 2\,H_2O \rightarrow 2\,Ni + BO_2^- + 4\,H^+ + 2\,H_2 \quad (2)$$

$$BH_4^- + H_2O \rightarrow B + OH^- + 2.5\,H_2 \quad (3)$$

Effect of the reaction temperature: In addition to the reactions performed at 80 °C, in which the nanostructure was examined as described above, the reaction was carried out at room temperature (22 °C) to examine any effect of temperature. In contrast to the reactions at the higher temperature, the reduction now did not lead to an immediate color change of the solution, indicating a slower reaction rate. The black color gradually developed over a period of approximately 2 min, leading to a nearly colloidal suspension. The as-made nanoparticles were examined by TEM, SAED, and EDS.

As shown in Figure 7a–c, these nanoparticles are around 60 nm in size, and each particle is an aggregate of smaller particles. These smaller particles themselves are again the

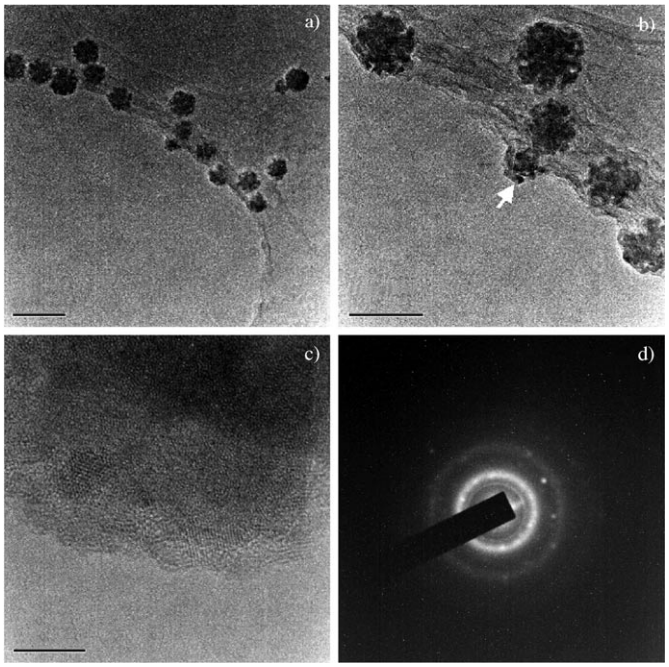

Figure 7. TEM images of the Ni–B nanoparticles produced at room temperature. a) Low and b) medium magnification images (scale bars: 200 nm and 100 nm, respectively); c) an HRTEM image shows the fine nanostructure of the particles in the edge area of the aggregate as indicated by the arrow in (b) (scale bar: 5 nm); d) SAED pattern recorded from the same area as shown by image (c).

aggregates of even smaller nanoparticles (1–3 nm). The whole assembly consequently displays a complex, blackberry-like morphology. As with the nanostructure observed earlier, a second amorphous phase is also found around the nanoparticles, appearing to cement them together. The recorded SAED pattern again shows the three prominent rings (Figure 7d), and the EDS analysis gives a very similar result as obtained previously. On the basis of these measurements, it is concluded that the nanostructure produced at room temperature is basically the same as that at higher temperature, except that at room temperature the aggregated nickel–boron component particles are less-tightly bound to each other.

Effect of the boron content: The presence of boron has been previously shown by chemical analyses,[9–11] and its content has been reported to vary with the ratio of reactants used in preparation.[7–18] However, how the boron content affects the Ni·B nanostructure has been scarcely studied. To better understand this, a comparative study of samples with varied boron content has been made. As can be seen from the HRTEM images shown in Figure 8, a higher content of

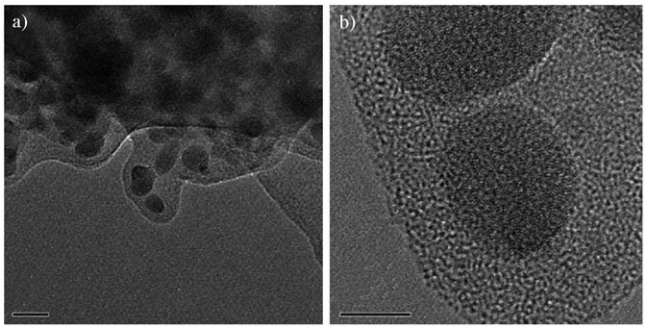

Figure 8. a) Low- and b) high-magnification TEM images of the nickel–boron nanoparticles prepared in the excess of boron, to show the amorphous boron coating on the particle surface (scale bars: 20 nm and 5 nm, respectively). In this case, the molar ratio of the nickel acetate to sodium borohydride was 1:3.

boron led to a much thicker amorphous coating on the particle surface. This amorphous coating existed on almost all of the particles, and some degree of crystallization within it could be induced upon prolonged exposure to the electron beam. Multiple EDS measurements indicated that in the original specimen with a reactant molar ratio of 1:1, a mean value of the O(K edge)/B(K edge) intensity ratio was approximately 1.1. The specimen precipitated with an excess of $NaBH_4$ (in this case, the molar ratio of Ni-$(CH_3COO)_2{\cdot}4\,H_2O$ to $NaBH_4$ was 1:3), however, showed an even smaller O(K edge)/B(K edge) ratio of approximately 0.8, implying a higher boron content. This, coupled with the large difference of the HRTEM image contrast between the amorphous shell and the crystalline core, confirmed that the shell was definitely a boron-containing species, and that increasing the boron content increased the thickness of this coating accordingly. However, the crystalline structure of the nickel core remained unchanged since faint, superimposed lattice fringes could still be discerned in the cores of the particles.

Effect of the surfactant—formation of the nickel–boron colloids: For comparison with the original precipitate, a colloidal Ni·B suspension was made by extending the reduction using sodium dodecylbenzene sulfonate (SDBS,

$C_{13}H_{29}SO_3Na$) as a surfactant. Examination of the colloidal particles by TEM showed that they were about 20–30 nm in size, with a similar morphology to that of the normally used colloidal nickel (Figure 9a and b). However, close inspection

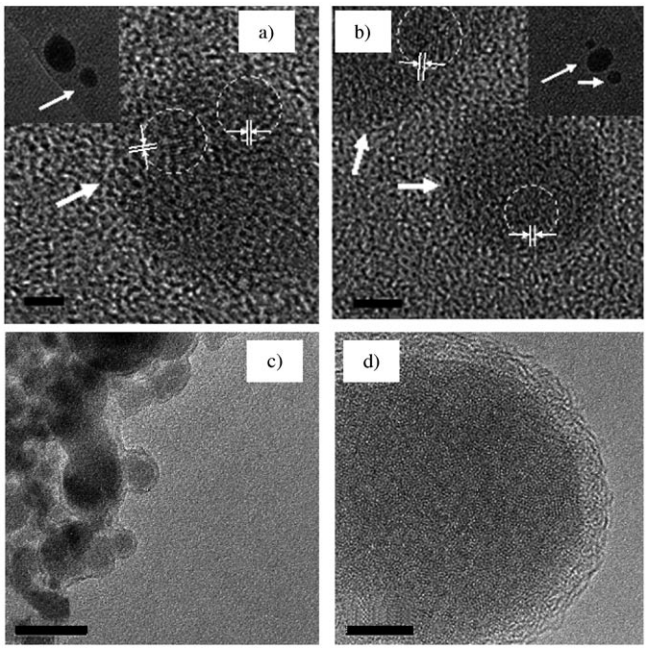

Figure 9. HRTEM images of the Ni–B colloids. a), b) The images of the as-made particles to show the unusual nanostructure; the lattice fringes from the component crystals with different orientations can be seen in these images (scale bars: 2 nm). c) A typical image shows that following the aging of the specimen for over two months, the nanoparticles developed a core–shell structure that is in a marked contrast to the original sample (scale bar: 50 nm). d) A HRTEM image of a core–shell nanostructure (scale bar: 5 nm).

by HRTEM revealed that these two forms of colloids were very different. In our specimen, the nanoparticles were not single crystals, but instead were composed of very small crystallites (up to $\approx$2 nm) and a second amorphous phase within their gaps. In comparison to the core–shell structure of the Ni•B precipitate, here no amorphous shell appeared to be on the surface. However, after aging the sample for over two months an examination showed that an amorphous coating was present (Figure 9c and d), which implied that some sintering had occurred in the aging period that had led to the development of the shell. Although the exact process is not yet clear, it is suspected that this change might be driven by a diffusion-related process in which the nickel and boron sintered, separately, with their neighboring species. As a consequence, the surface of the particles eventually became boron rich while the core was nickel rich.

Similar to the case in the precipitate, the recorded XRD profile of the colloids showed a weak but broad peak around $2\theta = 45°$, matching the diffraction of metallic Ni(111) (see Figure 2 in the Supporting Information). Almost certainly, the weakness and broadness of this diffraction reflect the nature of the extremely small size of the component crystals. Thermal treatment of the sample at 600 °C in argon yielded three strong diffractions corresponding to the peaks at $2\theta = 44.5$, 51.7, and 76.8° that match the diffractions of metallic nickel at Ni(111), Ni(200), and Ni(220), respectively.[33] In addition, EDS measurements clearly indicated the presence of both Ni and B (see Figure 3 in the Supporting Information). A trace amount of oxygen was also detected, which was believed to arise from the oxygen atoms of the surfactant molecules and the oxidation of the surface of the sample in air. No boron oxide was found as the measured mean O(K edge)/B(K edge) ratio was only approximately 1.5, which was far smaller than that of B_2O_3, approximately 13.9, under identical conditions. It is thus concluded that although the surfactant has little effect on the particle structure, it does modify the surface morphology.

The SAED pattern of an aggregate of the colloids is shown in Figure 10a. In this pattern, only one diffraction ring was observed, and it is clearly made up of many spots. Using the diffraction pattern of colloidal gold as a reference, we determined that this strong diffraction corresponded to a

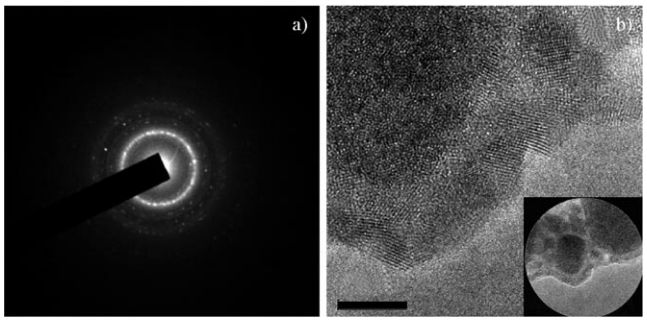

Figure 10. a) SAED pattern of the Ni–B colloids. b) The inset shows the selected area for the diffraction, whereas image (b) itself is an HRTEM image of part of the area to show the fine nanostructure (scale bar: 5 nm).

d spacing of approximately 2.1 Å, very close to that of the bulk Ni(111) (2.02–2.04 Å) but much less than that of the corresponding planes of NiO. Bearing in mind the lack of any appreciable oxygen peak in the EDS spectrum, we may therefore conclude that the nickel involved is not in the oxide form, which is consistent with the HRTEM observations and the XRD studies.

One question remains, namely the absence of other expected diffraction rings from metallic nickel. Some light may be shed on this by considering the ordering state of the nickel nanoparticles. The lowest-angle diffraction maximum of nickel is of (111), which results only from the presence of closely packed layers of atoms. The other diffraction maxima that we might expect to observe, namely (200), (220), and (311), all require a regular layer stacking sequence of ABCABC and so forth from the *fcc* structure. If any stacking faults are present, these latter beams will be broadened to the extent that they may not be visible. Given the extremely small size of the individual nickel crystallites, with the consequent likelihood of icosahedron-like struc-

tures being present,[36,37] it is not surprising that they are not observed. Indeed, at such small dimensions the particles may well be fluxional, so that only the interlayer correlations are preserved, and therefore only the (111) beam can be observed. The slight increase in spacing of the (111) planes when compared with bulk metal is to be expected, as some degree of structural relaxation is almost certainly present, and if the layers are effectively in motion, their spacing will be larger.

Another question that then arises is the origin of the other spots in the pattern, which cannot be indexed on the nickel unit cell. The area used to generate the SAED pattern is shown as an inset of Figure 10b and a portion of it is shown in an enlarged form in Figure 10b itself. The embryonic lattice fringes of the metallic nickel are clearly visible in the particle core, but so are many crystalline regions in the largely amorphous shell. It is not possible in the present work to identify the chemical composition of these small crystals on the shell [some clues may be seen from the kinetic reactions shown in Eqs. (1)–(3)]. However, they are clearly crystalline, and would certainly be expected to give rise to the diffraction spots that cannot be accounted for by metallic nickel.

Stabilizing the nickel–boron colloids: A prolonged exposure of the colloidal particles to water may cause a disappearance of the characteristic black color even though the sample is protected by an inert gas such as N_2. A light green solution containing Ni^{2+} ions may re-form, implying reoxidization of the Ni particles by H_2O, so that the formed Ni^{2+} ions are able to react with $NaBH_4$ again to yield a new colloidal suspension. This reversible process may be simply expressed by the following formula: Ni^{2+}/BH_4^- (aqueous)$\Leftrightarrow$Ni/B (solid suspended in H_2O). However, we found that the unstable Ni•B nanoparticle product could be converted into a more stable form. This change was achieved by precipitating the particles by using centrifugation and then redispersing them into an organic solvent. We noticed that although a number of polar solvents such as CH_2Cl_2, CH_3OH, or CH_3CH_2OH could serve as the redispersing solvent, in most cases the reformed suspension was not stable, as shown by a spontaneous precipitation appearing again over a period of time. However, when absolute ethanol or ethylene glycol was used, a stable suspension formed. In one of the latter samples, no precipitation was observed in more than one year (Figure 11a). In Figure 11b and c the TEM images of the redispersed and thus stabilized colloids are shown. In these images the core–shell nanostructure of the Ni•B nanoparticles can clearly be seen.

Effect of the reaction medium—formation of pure nickel single nanocrystals: In clear contrast to the product synthesized in aqueous solution, the reduction of $Ni(CH_3COO)_2{\cdot}4H_2O$ by $NaBH_4$ in absolute ethanol yielded pure nickel nanoparticles in the form of single crystals. This was revealed by HRTEM examinations (Figure 12a and b), in conjunction with the SAED and EDS analyses. These

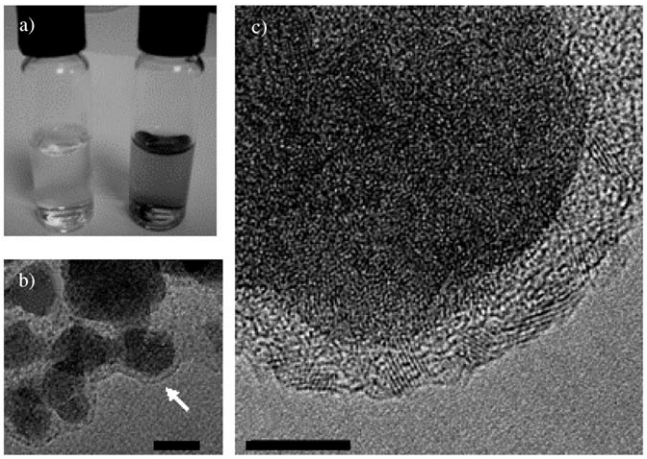

Figure 11. a) A photo shows a comparison between two samples: the original colloidal Ni–B aqueous suspension after aging for a week (left vial), which shows the disappearance of the black color of the suspension; and the re-treated sample by centrifugation and redispersion in ethanol after aging for over one year, showing the extremely good stability of the sample (right vial). b) A TEM image of the re-treated Ni–B nanoparticles. Scale bar: 20 nm. c) An HRTEM image of the particle, as shown in (b) by the arrow, indicates the core–shell nanostructure. Scale bar: 5 nm.

nanocrystals are extremely small, with a typical size of approximately 2 nm, and readily aggregate to form a precipitate. However, by using the SDBS surfactant, we prepared a colloidal nickel nanocrystal suspension (Figure 12c and d).

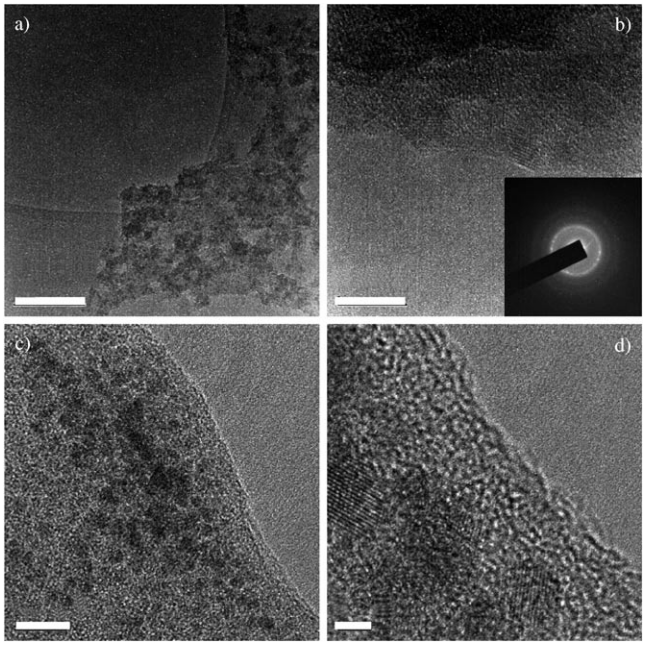

Figure 12. TEM images of the metallic Ni nanoparticles synthesized in ethanol. a) Low- and b) high-magnification images of the particles in the form of aggregates, and produced without using a surfactant (scale bars: 100 nm and 5 nm, respectively). c) Low- and d) high-magnification images of the particles in the form of single nanocrystals, and prepared by using the SDBS surfactant (scale bars: 10 nm and 2 nm, respectively).

These colloids are again very small, almost uniform in size, with a typical dimension of approximately 3 nm. The lattice fringes of individual crystals with $d \approx 2.0$ Å, corresponding to the Ni(111) plane, can be seen in the image. Due to a different reaction mechanism in ethanol, almost no boron was produced. In addition, these pure metallic nickel colloids were air-insensitive.

It was noticed that a small amount of water was naturally introduced into the reaction system from the reactant, $Ni(CH_3COO)_2 \cdot 4H_2O$, as it contained crystalline water. This small amount of H_2O might have assisted the dispersion of the Ni nanocrystals in ethanol because water could improve the dissolution capacity of the ionic SDBS surfactant. This in turn favored the stabilization of the Ni particles. The crystalline H_2O accounts for 28.9 wt% of the overall molecular weight. In a typical reaction, 508 mg nickel acetate was dissolved in 60 mL ethanol, which could introduce 147 mg H_2O into the reaction system.

Relation between the catalytic activity and the structural characteristics—a discussion: The high catalytic activity of Ni•B for hydrogenation and dehydrogenation reactions would appear to be related to the existence of boron in the material. However, the exact nature of the interaction between nickel and boron within the nanoparticles is not yet clear, although a fuller understanding is vital if the catalytic activity is to be understood. It has been observed that in hydrocarbon reactions using transition metals as catalysts, the catalyst deactivation due to carbon deposition on the metal is an important limitation in their application.[41–44] This sort of deactivation, commonly termed as the "coking effect", is caused by the catalytic dehydrogenation of hydrocarbons, $C_mH_n \rightarrow m\,C + {}^1/_2 n\,H_2$. The coking of a Ni-based catalyst is particularly problematic because of the rapid carbon-deposition rate as observed in hydrogenation reactions and the growth of carbon nanotubes.[45,46] It is therefore frequently necessary to add a catalytic promoter to improve the coking resistance of a Ni-based catalyst.

It has been indicated by Chen et al. that adding boron to a nickel catalyst can improve the coking resistance during the catalytic partial oxidation of methane.[47] In this case, boron is believed to act as a structural promoter that helps to reduce the size of the Ni particles and increase their thermal stability. A more recent theoretical study by Xu and Saeys using first-principles density functional theory calculations suggests that a small amount of boron corresponding to a single monolayer adsorption may be sufficient to reduce the coking of a Ni-based catalyst.[48] This is largely because boron prefers to adsorb in the octahedral sites of the first subsurface layer of the metal so that the boron atoms effectively block the subsurface sites and thus prevent carbon diffusion into the bulk of the metal. This effect assists in forcing carbon atoms to be available on the surface for reactions.

It has also been suggested that electrons are transferred from B to Ni, which is based on the changes of the binding energies of B 1s as detected by the XPS measurements.[9,12,14,30] However, no appreciable change of the binding energy of Ni 2p has been detected. This suggests that the view of the electron transfer, noted as Ni←B, may be wrong or only partially correct. From a chemical standpoint, it is hard to accept this view because boron has a higher electronegativity than nickel (χ_B, 2.04; χ_{Ni}, 1.91).[38] A plausible interpretation of the XPS result may instead be that the increase in the binding energies of B 1s only indicates that electrons have been withdrawn from boron atoms, but this does not necessarily mean that these charges should go to the nickel. In fact, the kinetic equations describing the solution reactions [see Eqs. (1)–(3)] indicate that these electrons may go to the nearest oxygen-containing species due to formation of the BO_2^- ions. Nevertheless, the XPS observations of the unchanged binding energy of Ni 2p is in good agreement with our HRTEM studies, and supports our conclusion that the component crystalline nanoparticles in the Ni•B material are pure metallic nickel.

Our HRTEM observations also indicate that the very small Ni crystallites are clearly covered by an amorphous B-containing species, which may prevent the sintering of the crystals on the one hand, but reduce the number of active sites in catalysis on the other. This result may be compared with a comparative study of the catalytic properties of $Ni_{68}B_{32}$ and pure nickel for the hydrogenation of ethylene, in which the measured pre-exponential factor (A_s) derived from the Arrhenius equation is nearly two orders of magnitude smaller than that of pure metallic nickel (Ni powder, 9.5×10^5; $Ni_{68}B_{32}$, 1.5×10^4).[39] Since the pre-exponential factor provides an insight into the number of active sites associated with the reaction rate, the lower A_s value indicates that the number of active sites in the Ni•B species is rather low, which suggests a low concentration of surface Ni atoms presumably due to the enrichment of the B-containing species on the surface. However, the measured apparent activation energy (E_a) of the Ni•B species is low as well (Ni powder, 34 kJ mol^{-1}; $Ni_{68}B_{32}$, 12 kJ mol^{-1}),[39] which indicates an opposite and promoting effect of boron for the hydrogenation.

On the basis of these experiments, it seems reasonable to argue that the high catalytic activity of the Ni•B nanoparticles should result from the high dispersion and thus extremely small size of the component Ni crystals owing to the sintering-inhibition effect caused by the amorphous boron-containing species. On the other hand, the coking resistance of nickel may have been effectively improved because of the subsurface layer adsorption of boron on the metal. It seems unlikely for the high catalytic activity to arise from any possible increase of the number of active sites or electron transfers. When Ni nanocrystals have a very small size down to approximately 1 nm, the surface electronic state of the metal must be dramatically different from that of the bulk, and a much higher surface energy or activity is thereby expected. Furthermore, these very small nickel particles may constantly keep changing in their shape and undergo rapid structural rearrangements, as suggested by the SAED measurements in this work, and also indicated by the studies

of the growth of carbon nanotubes using nickel nanoparticles as catalyst.[40] As a consequence, the metal may display continually renewed surface with time, therefore acting as a constant supply of active sites for catalysis. In addition, when the Ni•B nanoparticles produced in different reduction media (either in an aqueous solution or in ethanol) are considered,[2–6] their different catalytic properties for a given hydrogenation reaction may be explained in terms of their very different nanostructures and compositions, and this has been clearly shown by our characterization results.

Conclusion

To the best of our knowledge, this work provides the first systematic study of using HRTEM to observe the ultrafine nanostructure of the nickel–boron catalyst. Unlike the earlier suggestion that this material is amorphous, our studies indicate that it is not amorphous but actually possesses a highly unusual nanostructure that is made up of tiny nickel nanoparticles (1–3 nm) bound in a matrix of a boron-containing species. Almost certainly, the boron acts as a "cement" to hold the nanoparticles together, and prevents their sintering. This interesting combination of the two elements allows the nickel particles to remain extremely small in size, with a consequent very high surface area, hence offering an explanation as to why the catalyst is exceedingly active over a wide range of hydrogenation reactions. Since studies on this Ni•B system have been widely extended to other metal–metalloid materials, our findings provide useful insights into the understanding of the fascinating ultrafine structures of similar nanoalloys. In addition, we consider that there should be strong magnetic dipolar interactions between the constituent nickel crystallites because of their extremely small size and their highly tightly bound nature. This may provide an opportunity to investigate new magnetic properties of these bi-elemental quantum dots, in particular, when the collective properties are possibly tuned by changes in the boron content.

Experimental Section

Synthesis: The nickel–boron catalytic precipitate was synthesized by the reduction of nickel acetate with sodium borohydride in aqueous solution. The reactions were carried out at room temperature (21 °C) and a higher temperature (80 °C), with varied molar ratios between the metal salt and the borohydride. For a typical reaction, a solution of Ni-$(CH_3COO)_2$•$4H_2O$ (452 mg; Aldrich Chemicals, 99.9 %) was treated with $NaBH_4$ (160 mg; Lancaster, 98 %) in a Schlenk flask under vigorous stirring. The solution turned black almost immediately after mixing the two reagents, which indicated the formation of the nickel–boron nanoparticles. For the higher temperature reactions, the solution was allowed to cool down when the hydrogen evolution ceased. The product was a precipitate obtained over a period of approximately 20 h. The nickel–boron colloids were synthesized by extending the reaction method and using sodium dodecylbenzene sulfonate ($C_{18}H_{29}SO_3Na$, SDBS; Acros Organics, 88 %) as a surfactant. To ensure the reduction of the salt was complete, the employed borohydride was slightly in excess with respect to the stoichiometric ratio. A typical molar ratio of the reactants was Ni-$(CH_3COO)_2$•$4H_2O$/$NaBH_4$/SDBS = 1:2.1:0.6. Instead of having a precipitate as the product, the reaction yielded a colloidal suspension. The particles in the suspension could be precipitated out by centrifugation. The pure metallic nickel colloids in the form of single nanocrystals were made under inert gas (Ar) by following the same reaction route. In this case, instead of using the aqueous solution, absolute ethanol was used as the solvent for the reaction.

Characterization: SEM images were obtained from a LEO-32 electron microscope operated at 5 kV. Samples were directly deposited on a specimen holder (carbon mat) without surface coating of a conducting material. HRTEM observations were performed with a JEOL JEM-3011 electron microscope operated at 300 kV. Images were recorded at magnifications up to 1000000×. The TEM samples were deposited on Cu grids (400 mesh) with a holey carbon supporting film.

For the XRD studies, the precipitated sample was repeatedly washed with distilled water and ethanol and then dried under vacuum. The XRD patterns were recorded using a step size of 0.05° on a Philip Xpert spectrometer ($Cu_{K\alpha 1}$, $\lambda = 1.5418$ Å). The annealing treatment was carried out at 600 °C in argon. For performing the nano-beam electron diffractions, the camera was calibrated using equivalent diffraction patterns of colloidal gold, and care was taken to ensure a constant objective lens excitation, which ensures that there was no change in the focal length between different diffraction patterns. Only particles protruding over holes of the carbon/plastic support film were studied to eliminate any contribution of the amorphous carbon to the diffraction rings.

In the EDS analyses, given the relatively low detection rates at the low energy for the detection of boron, a standard deviation of around 10 % was probably the best accuracy that could be achieved. With the actual specimens, due to the superposition of the X-ray peaks from the amorphous coating of the particles and the supporting carbon film, the stronger carbon K emission partly masked the boron K emission line. A background subtraction was therefore necessary. This was done by recording a spectrum from a region of the specimen and then recording a second spectrum from an adjacent area of the carbon film so that the height of the carbon K emission peak was the same in both. Subtraction of the second from the first then produced a corrected spectrum. Fortunately, the spectrometer resolution at the low energies was approximately the same order of magnitude as the 92 eV separation of boron and carbon K emission lines, thus a correction was possible.

XPS spectra were obtained by using a VG Escalab MkII surface analysis system with $Al_{K\alpha}$ (1486.6 eV) incident radiation at normal take-off angle. Elemental compositions were approximately quantified (assuming a uniform composition over the XPS sampling depth) from XPS peak areas using literature relative sensitivity factors. Possible peak assignments were made by using the Perkin-Elmer Handbook of XPS.[49] The sample powder was mounted onto a tacky conductive carbon pad (some of the C signal may come from incomplete coverage by the powder as a result). The binding energy scale is referenced to the contaminant carbon (C 1s = 285.0 eV), and this scale is shifted very slightly such that the C–C C 1s peak falls at 284.6 eV.

Acknowledgements

We thank financial support from the EU EXCELL project. The JEM-3011 electron microscope and PGT Avalon 2000 EDS system were obtained by using EPSRC grant M51109.

[1] a) *Catalysis and Electrocatalysis at Nanoparticle Surfaces* (Eds.: A. Wieckowski, E. R. Savinova, C. G. Vayenas), Marcel Dekker, New York, **2003**,; b) V. Ponec, G. C. Bond, *Catalysis by Metals and Alloys*, Elsevier, Amsterdam, **1995**,.
[2] H. I. Schlesinger, H. C. Brown, A. E. Finholt, J. R. Gilbreath, H. R. Hoekstra, E. K. Hyde, *J. Am. Chem. Soc.* **1953**, *75*, 215.
[3] C. A. Brown, *J. Org. Chem.* **1970**, *35*, 1900.
[4] H. C. Brown, C. A. Brown, *J. Am. Chem. Soc.* **1962**, *84*, 1493.

[5] H. C. Brown, C. A. Brown, H. C. Brown, *J. Am. Chem. Soc.* **1963**, *85*, 1003.
[6] C. A. Brown, V. K. Ahuja, *J. Org. Chem.* **1973**, *38*, 2226.
[7] J. Y. Shen, Z. Y. Li, Q. J. Yan, Y. Chen, *J. Phys. Chem.* **1993**, *97*, 8564.
[8] R. N. Duncan, T. L. Arney, *Plat. Surf. Finish.* **1984**, *71*, 49.
[9] a) R. Paul, P. Buisson, N. Joseph, *Ind. Eng. Chem.* **1952**, *44*, 1006; b) P. C. Maybury, R. W. Michell, M. F. Hawthorne, *J. Chem. Soc. Chem. Commun.* **1974**, 534.
[10] a) Y. Chen, *Catal. Today* **1998**, *44*, 3; b) R. Paul, P. Buisson, N. Joseph, *Compt. Rend.* **1951**, *232*, 627.
[11] H. Li, H. Li, W. Dai, M. Qiao, *Appl. Catal. A* **2003**, *238*, 119.
[12] Y. Okamoto, Y. Nitta, T. Imanaka, S. Teranishi, *J. Chem. Soc. Faraday Trans. 1* **1979**, 2027.
[13] J. van Wonterghem, S. Morup, C. J. W. Koch, S. W. Charles, S. Wells, *Nature* **1986**, *322*, 622.
[14] J. A. Schreifels, P. C. Maybury, W. E. Swartz, Jr., *J. Catal.* **1980**, *65*, 195.
[15] R. C. Wade, D. G. Holah, A. N. Hughes, B. C. Hui, *Catal. Rev. Sci. Eng.* **1976**, *14*, 211.
[16] D. G. Holah, I. M. Hoodless, A. N. Hughes, L. Sedor, *J. Catal.* **1979**, *60*, 148.
[17] Y. C. Liu, C. Y. Huang, Y. W. Chen, *Ind. Eng. Chem. Res.* **2006**, *45*, 62.
[18] H. Li, H. Luo, L. Zhuang, W. Dai, M. Qiao, *J. Mol. Catal. B* **2003**, *203*, 267.
[19] a) J. Saida, A. Inoue, T. Masumoto, *Metall. Trans. A* **1991**, *22A*, 2125; b) S. Linderoth, S. Morup, *J. Appl. Phys.* **1991**, *69*, 5256.
[20] a) J. Y. Shen, Z. Y. Li, Q. J. Yan, Y. Chen, *J. Phys. Chem.* **1993**, *97*, 8564; b) J. Shen, Q. Zhang, Z. Li, Y. Chen, *J. Mater. Sci. Lett.* **1996**, *15*, 715.
[21] a) A. Inoue, J. Saida, T. Masumoto, *Metall Trans.* **1988**, *19A*, 2315; b) H. Wang, Z. Yu, H. Chen, J. Yang, J. Deng, *Appl. Catal. A* **1995**, *129*, L143.
[22] S. Mørup, S. A. Sethi, S. Linderoth, C. B. Koch, M. D. Bentzon, *J. Mater. Sci.* **1992**, *27*, 3010.
[23] G. E. Colfand, J. L. Garnett, *J. Phys. Chem.* **1964**, *68*, 3887.
[24] a) W. E. Truce, F. E. Roberts, *J. Org. Chem.* **1963**, *28*, 961; b) W. E. Truce, F. M. Perry, *J. Org. Chem.* **1965**, *30*, 1316.
[25] a) N. Sulitanu, I. Sandu, *Rev. Chim.* **2003**, *54*, 561; b) A. M. Bratkovsky, S. N. Rashkeev, A. V. Smirnov, G. Wendin, *Europhys. Lett.* **1994**, *26*, 43; c) A. M. Bratkovsky, S. N. Rashkeev, G. Wendin, *Phys. Rev. B* **1993**, *48*, 6260.
[26] J. E. Hofer, J. F. Shultz, R. D. Panson, R. B. Anderson, *Inorg. Chem.* **1964**, *3*, 1783.
[27] J. Deng, J. Yang, S. Sheng, H. Chen, G. Xiong, *J. Catal.* **1994**, *150*, 434.
[28] Y. He, M. Qiao, H. Hu, Y. Pei, H. Li, J. Deng, K. Fan, *Mater. Lett.* **2002**, *56*, 952.
[29] Y. Okamoto, Y. Nitta, T. Imanaka, S. Teranishi, *J. Chem. Soc. Faraday Trans. 1* **1980**, *76*, 998.
[30] J. Shen, Z. Hu, Q. Zhang, L. Zhang, Y. Chen, *J. Appl. Phys.* **1992**, *71*, 5217.
[31] J. Geng, D. A. Jefferson, B. F. G. Johnson, *Chem. Commun.* **2007**, 969.
[32] a) H. P. Erickson, A. Klug, *Philos. Trans. R. Soc. Lond. B* **1971**, *261*, 105; b) J. Frank, S. C. McFarlane, K. H. Downing, *Optik* **1978**, *52*, 49.
[33] The International Centre for Powder Diffraction Data, *Powder Diffraction Files* **2001**, Card Numbers: 87-0712, 45-1027, 04-0850, 03-1051, 03-1043, 01-1258.
[34] Three other weak diffraction peaks in the XRD spectrum, with $d=$ 2.09, 2.41, and 1.48 Å, respectively, correspond to NiO.[35] This was further confirmed by the EDS measurements coupled with their high-resolution TEM images. This oxide was believed to result from either the reaction of the component Ni crystals with the H_2O contained in the sample, to first form $Ni(OH)_2$, which subsequently decomposed into NiO at elevated temperatures, or the oxidation of the metal in air during the operation process.
[35] The International Centre for Powder Diffraction Data, *Powder Diffraction Files* **2001**, Card Numbers: 47-1049, 44-1159, 22-1189.
[36] M. B. Gordon, F. Cyrot-Lackmann, M. C. Desjonqueres, *Surf. Sci.* **1977**, *68*, 359.
[37] M. B. Gordon, F. Cyrot-Lackmann, M. C. Desjonqueres, *Surf. Sci.* **1979**, *80*, 159.
[38] a) L. Pauling, *The Nature of the Chemical Bond*, 3rd ed., Cornell University Press, Ithaca, **1960**; b) *Handbook of Chemistry and Physics*, 84th ed. (Ed.: D. R. Lide), CRC Press, **2003–2004**, pp. 9–76.
[39] W. S. Xia, Y. Fan, Y. S. Jiang, Y. Chen, *Appl. Surf. Sci.* **1996**, *103*, 1.
[40] S. Helveg, C. Lopez-Cartes, J. Sehested, P. L. Hansen, B. S. Clausen, J. R. Rostrup-Nielsen, F. Abild-Pedersen, J. K. Norskov, *Nature* **2004**, *427*, 426.
[41] J. C. Vedrine, G. Hollinger, T. M. Duc, *J. Phys. Chem.* **1978**, *82*, 1515.
[42] R. W. Joyner, G. R. Darling, J. B. Pendry, *Surf. Sci.* **1988**, *205*, 513.
[43] M. C. Zonnevylle, J. J. C. Geerlings, R. A. Van Santen, *Surf. Sci.* **1990**, *240*, 253.
[44] J. R. Rostrup-Nielsen, P. Højlund Nielsen, *Deactivation and Poisoning of Catalysts* (Eds.: J. Oudar, H. Wise), Dekker, New York, **1985**.
[45] H. S. Bengaard, J. K. Nørskov, J. Sehested, B. S. Clausen, L. P. Nielsen, A. M. Molenbroek, J. R. Rostrup-Nielsen, *J. Catal.* **2002**, *209*, 365.
[46] a) J. Geng, S. Hofmann, V. B. Golovko, B. Kleinsorge, C. Ducati, D. S. Shephard, J. Robertson, B. F. G. Johnson, *J. Phys. Chem. B* **2004**, *108*, 18446; b) J. Geng, B. F. G. Johnson, D. A. Jefferson, *J. Mater. Chem.* **2005**, *15*, 844.
[47] L. Chen, Y. Lu, Q. Hong, J. Lin, F. M. Dautzenberg, *Appl. Catal. A* **2005**, *292*, 295.
[48] J. Xu, M. Saeys, *J. Catal.* **2006**, *242*, 217.
[49] C. D. Wagner, W. M. Riggs, L. E. Davis, J. F. Moulder, *Handbook of X-ray Photoelectron Spectroscopy*, 1st ed. (Ed.: G. E. Muilenberg), Perkin-Elmer Corporation (Physical Electronics Division), Eden Prairie, MN (USA), **1979**.

Received: June 11, 2008
Revised: August 28, 2008
Published online: December 16, 2008

